I&EC research
Industrial & Engineering Chemistry Research

Article

Cite This: Ind. Eng. Chem. Res. 2019, 58, 1167−1176

pubs.acs.org/IECR

Continuous Synthesis of Structurally Uniform Graphene Oxide Materials in a Model Taylor−Couette Flow Reactor

Mohammed AlAmer,[†] Ae Ran Lim,[‡,§] and Yong Lak Joo*[,†]

[†]Robert Fredrick Smith School of Chemical and Biomolecular Engineering, Cornell University, Ithaca, New York 14853, United States

[‡]Analytical Laboratory of Advanced Ferroelectric Crystals, and [§]Department of Science Education, Jeonju University, Jeonju 55069, South Korea

ABSTRACT: Graphene oxide (GO) has proven to be an invaluable material for a wide range of applications. The development of a bulk-scale continuous process to synthesize GO materials has become crucial. In this study, we used a model Taylor−Couette reactor with axial flow to transform the oxidation of graphite flakes into a continuous process. Efficient mixing of graphite and oxidizing agents was achieved via Taylor vortices, which remarkably shortened the duration of graphite oxide (GtO) synthesis from hours to minutes. Our results reveal that the level of oxidation increased at the Taylor vortex flow (TVF) regime and significantly decreased at other hydrodynamic flow regimes. More importantly, TVF regime resulted in structurally uniform GtO products. This confirms that the developed apparatus offers a robust method to synthesize high-quality, structurally uniform GtO in a continuous manner that can be used in numerous applications.

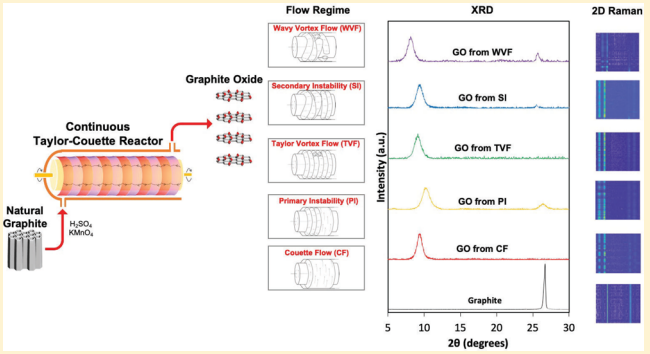

1. INTRODUCTION

Reliance on depleting fossil fuels along with the associated environmental concerns has urged the development of sustainable energy resources. This led to a rising demand for advanced energy storage units suitable for electric vehicles and intermittent renewable energy resources. Lithium-ion batteries (LIBs) have been receiving unprecedented attention as the leading power source of choice for sustainable energy due to their high voltage, low self-discharging rate, long cycling life, low toxicity, and high reliability.[1] Nonetheless, LIBs are reaching their performance limit, which is highly dependent on the choice of electrode materials. This led to an increased demand for a newer generation of LIBs.[2] Conventional LIBs consist of a graphite anode, a lithium metal oxide cathode (e.g., $LiCoO_2$), and an electrolyte containing a solution of a lithium salt (e.g., $LiPF_6$) imbedded in a separator membrane.[3] Recently, silicon (Si) has attracted attention as an emerging alternative to graphite (372 mAh/g) for anodes in LIBs due to its high theoretical specific capacity (∼4200 mAh/g) corresponding to the formation of $Li_{22}Si_5$ alloy.[4,5] However, its potential has been limited given the massive volume expansion (>300%) during charging/discharging cycles, resulting in structural crumbling and particle cracking, especially at higher currents.[5−8] This also led to loss of electrical contact and capacity fading.[5,6,9,10] Xiang and his co-workers prepared graphene/nanosized Si composites by homogeneously mixing graphene oxide (GO) and nanosized Si particles in an aqueous solution and annealing the samples at 500 °C to yield thermally reduced GO and nanosized Si composites. The addition of graphene materials to the composites proved to effectively enhance the cycling stability of Si anode in LIBs.[11,12]

Graphene has attracted massive attention in the past decade due to its large theoretical surface area (>2600 m^2/g),[13−15] high electrical conductivity,[16] mechanical robustness,[17] and ease of surface modification.[18] Graphene has also been used as a coating for other materials to enhance their properties while maintaining the properties of the underlying material.[1,19,20] Graphene could be prepared by the oxidation of graphite in the presence of strong acids and oxidizing agents to produce graphite oxide.[17] Graphene could also be synthesized via other top-down approaches such as mechanical exfoliation known as the "Scotch tape" or peel-off method.[13,21] Bottom-up routes can also be used to produce graphene, such as chemical vapor deposition (CVD) and epitaxial growth on silicon carbide substrates.[22−25]

GO was mainly produced by the Brodie,[26] Staudenmaier,[27] and Hummers[28] methods. Hummers and his co-workers synthesized graphene by deep oxidation of natural graphite flakes to form graphite oxide, followed by the sonication of graphite oxide to produce GO. GO is then reduced, either

Received: September 11, 2018
Revised: December 11, 2018
Accepted: December 14, 2018
Published: December 14, 2018

DOI: 10.1021/acs.iecr.8b04428
Ind. Eng. Chem. Res. 2019, 58, 1167−1176

chemically or thermally, to yield graphene sheets. The two-step oxidation method uses an anhydrous mixture of sulfuric acid (H_2SO_4), sodium nitrate ($NaNO_3$), and potassium permanganate ($KMnO_4$), which are mixed at three different temperature stages, followed by the addition of deionized (DI) water to complete the second oxidation stage, and finally the addition of hydrogen peroxide (H_2O_2) to terminate the oxidation reaction.[28] There are a number of variations of Hummer's oxidation method using different oxidants and temperature stages. For example, Tour and his co-workers investigated the addition of phosphoric acid (H_3PO_4), which has improved the efficiency of the oxidation process, increased the viscosity of the reaction medium, eliminated the generation of toxic gases (NO_2 and N_2O_4), and resulted in an easily temperature-controlled reaction medium.[29] Chen and his co-workers concluded that eliminating $NaNO_3$ would also result in a simplified waste disposal because of the inexistence of Na^+ and NO_3^- ions. Their method resulted in a lower content of Mn^{2+} ions in the purified wastewater.[30] Shahriary and his co-worker synthesized GO at a lower temperature (35 °C) and a longer reaction time (12 h).[31] Since the oxidation step in the Hummer's method is mass-transfer limited, Park and his co-workers used a batch Taylor−Couette reactor (TCR), which generated turbulent Taylor vortices that enhanced the mixing and mass transfer of graphite and the oxidizing agents. This revolutionized the synthesis of graphite oxide (GtO), as the time length of the first oxidation step was shortened from 4 h to 30 min.[32] Taylor−Couette flow was named after the works by G. I. Taylor[33] and M. Couette.[34] TCR consists of two coaxial cylinders with the inner one rotating while the outer one is still, creating toroidal vortices, or Taylor vortices, resulting in efficient radial mixing of the reaction medium.[35] Couette was the first to observe that the torque needed to rotate the outer cylinder while the inner cylinder is stagnant and increases linearly with the rotation speed. After reaching a critical rotation speed, the torque increased more rapidly as the flow observes an instability, where the flow is transitioned from stable to unstable.[34] Taylor observed flow instability between two concentric rotating cylinders. Taylor succeeded in applying linear stability theory for viscous flow and compared the results to flow pattern observations. When the rotation of the inner cylinder is low, the flow remains laminar, or Couette flow (CF). When the rotation speed of the inner cylinder exceeds a critical value, a primary flow instability is observed, and stable vortices, or cellular rolls, are developed. This flow pattern is called the Taylor vortex flow (TVF). When the rotation of the inner cylinder increases and reaches a secondary critical value, a secondary flow instability is observed. The cellular vortices break down and a turbulent pattern is developed, where vortices' boundaries are wavy. This flow pattern is called the wavy vortex flow (WVF).[33] TCR flow regime has been extensively studied to investigate the effects of mixing and axial dispersion in a number of applications.[33−40] Aljishi and his co-workers studied the effect of vortex flow in a Taylor−Couette crystallizer on the precipitation of barium sulfate crystals and how different flow regimes could impact the crystal properties.[36] Nguyen and his co-workers employed a continuous TCR to study the effect of Taylor vortices on the phase transformation of guanosine 5-monophosphate (GMP). Intensive mixing in the TCR resulted in the growth of the hydrate GMP crystals within a mean residence time of 5 min, which is at least five times faster than phase transformation observed in conventional crystallizers under the same crystallization conditions.[41]

In this investigation, we report the synthesis of graphite oxide using a continuous flow TCR with dimensionless control parameters, namely, the Reynolds number and the Taylor number. The results will be discussed in terms of yield of graphite oxide. The reported new method significantly shortens the reaction time with promising GtO yields. The TCR employed for this method creates different flow regimes to effectively mix graphite with strong oxidizing agents (H_2SO_4 and $KMnO_4$). We will demonstrate that the level of oxidation strongly depends on flow structure, and continuous Taylor vortex flow regime resulted in a structurally uniform graphite oxide product.

2. EXPERIMENTAL SECTION

2.1. Materials. Natural graphite powders were obtained from Asbury Carbon (230U, 25−45 mesh). Concentrated sulfuric acid (H_2SO_4) (cat# 470302-872) and 30% hydrogen peroxide (H_2O_2) (cat# BDH7742-1) were purchased from VWR and used as provided. Potassium permanganate ($KMnO_4$) (cat# 223468) and 37% hydrochloric acid (HCl) (cat# 258148) were purchased from Sigma-Aldrich and used as provided. Deionized (DI) water was used during all of the syntheses.

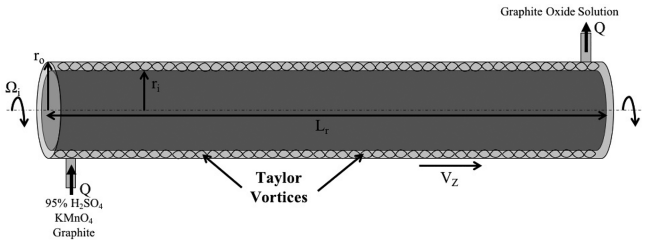

Figure 1. Schematic of graphite oxidation in a Taylor−Couette reactor system.

Table 1. Dimensions of Taylor−Couette Reactor

r_i (cm)	r_o (cm)	$d(r_o - r_i)$ (cm)	L_r (cm)
2.29	2.54	0.25	30.48

2.2. Experimental Setup. The experimental setup of the TCR, illustrated in Figure 1, consisted of two coaxial bronze cylinders, with the inner one rotating while the outer one is still. The inner cylinder rotation rate is controlled by a phase inverter, connected to a motor drive that provides rotation rates in range of 30−1500 rpm. Table 1 includes the physical specifications of the TCR used in the current study, where r_i and r_o are the inner and outer cylinder radii, respectively, d is the corresponding gap width, and L_r is the length of the TCR. Aljishi and his co-workers characterized a TCR system with the same dimensions reported in Table 1 and determined that the presence of axial flow delays the formation of instabilities.[36] The TCR system is driven through the rotation of the inner cylinder, which is quantified in dimensional form of the inner cylinder's angular velocity Ω_i and in dimensionless form by the Reynolds number Re_i based on the inner cylinder rotation

$$Re_i = \frac{r_i \Omega_i d}{\nu} \quad (1)$$

DOI: 10.1021/acs.iecr.8b04428
Ind. Eng. Chem. Res. 2019, 58, 1167−1176

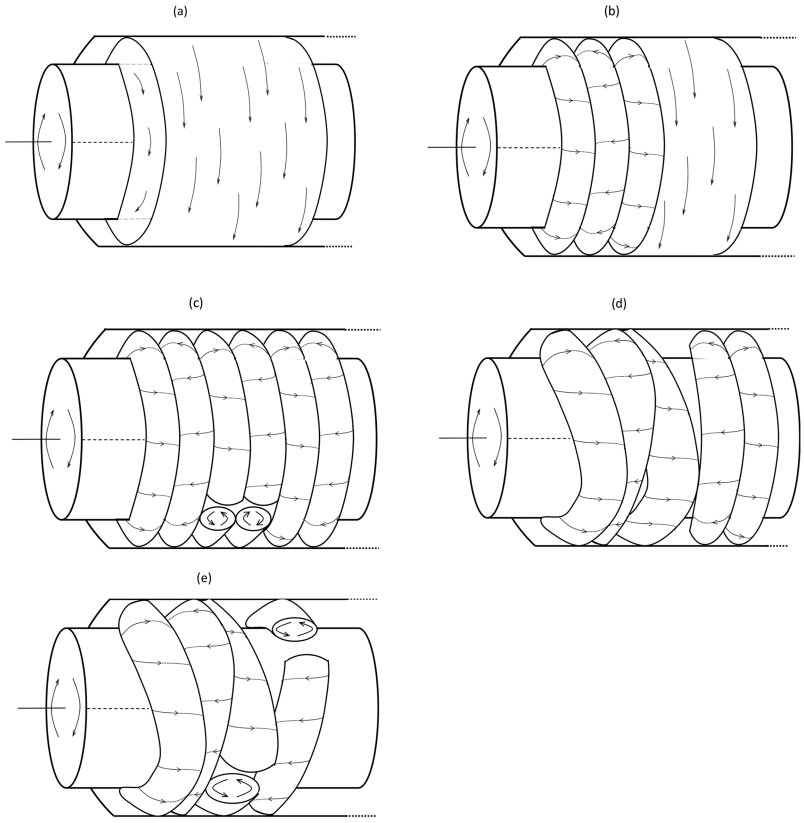

Figure 2. Hydrodynamic flow regimes in TCR: (a) CF, (b) PI, (c) TVF, (d) SI, and (e) WVF.

where ν is the kinematic viscosity of the Newtonian fluid between the two cylinders. The viscosity is determined by Einstein's formula based on the volume fraction of suspended particles for heterogeneous mixtures.[42] The hydrodynamic instabilities are determined by the critical Taylor number ($Ta_{c,i}$), where i corresponds to the instability (i = 1 for the primary instability between laminar CF and TVF and i = 2 for the secondary instability between TVF and WVF). In order to characterize the TCR flow regime, one can use the Taylor number Ta

$$Ta = \frac{2r_i^2 d^4}{(r_o^2 - r_i^2)}\left(\frac{\Omega_i}{\nu}\right)^2 \quad (2)$$

The superimposed axial flow is characterized by the axial Reynolds number Re_z

$$Re_z = \frac{V_z d}{\nu} = \frac{Qd}{A\nu} = \frac{Q}{\pi(r_i + r_o)\nu} \quad (3)$$

where V_z is the mean axial velocity, Q is the flow rate, and A is the cross-sectional area of the channel. The viscosity used for the calculation of Ta and Re_z is the viscosity at the inlet, which determines the flow condition at the inlet. The scope of this study involved oxidizing natural graphite flakes under laminar CF ($Ta < Ta_{c,1}$), TVF ($Ta_{c,1} < Ta < Ta_{c,2}$), and WVF ($Ta > Ta_{c,2}$) with Re_z = 7.9 (mean residence time ~75 s). It should be noted that $Ta_{c,i}$ is adjusted to accommodate for the presence of axial flow, which causes the system to become more stable and significantly delay the onset of instability, as the increase in axial flow diminishes the dominance of centrifugal forces.[36,39] The determination of the Taylor number is affected by the gradual change in viscosity of the fluid medium in the TCR given that the viscosity of the fluid medium changes as the feed solutions enter the reactor, which results in an uncertainty in the pumping flow. Park and his co-workers have demonstrated how using a TCR would almost double the viscosity of the reaction medium in comparison to the conventional Hummers method. A residence time of 75 s in the TCR would increase the viscosity of the mixture at the inlet by almost 5%.[36,43] We determined the effective Reynolds and Taylor numbers based on the apparent viscosity at the inlet (before the reaction) and at the outlet (after the reaction) to represent the change in viscosity and Reynolds and Taylor numbers in the reactor.

2.3. Graphite Oxide (GtO) Synthesis. GtO was prepared according to the Hummer's method. Modifications in the synthesis method were performed to understand the parameter that could affect the quality of the synthesized material. Graphite (4 g) was suspended in 120 mL of concentrated sulfuric acid in an ice bath (0 °C) in a 250 mL round-bottom flask equipped with a magnetic stir bar. The obtained solution was stirred for 10 min. Then, 12 g of $KMnO_4$ was slowly added, and the stirring continued for 30 min. The mixture solution was transferred to a TCR using a peristatic pump with a pumping rate of 1.6 mL s^{-1}. The mixture solution was introduced into the gap between the two cylinders while the inner cylinder was rotating under room temperature. The rotation speed of the inner cylinder was varied from 290 to 600 rpm. The rotation of the inner cylinder while the outer cylinder is stationary induces highly effective radial mixing, an enhanced mass transfer of the reactants, and a high wall shear stress, which strongly improves the rate of mass transfer of the oxidizing agents into the graphite interlayer and exfoliates graphene sheets.[32] Then, the solution was transferred to a room-temperature water bath, and 120 mL of DI water was

DOI: 10.1021/acs.iecr.8b04428
Ind. Eng. Chem. Res. 2019, 58, 1167−1176

added slowly into the solution. After that, 12 mL of H_2O_2 was added slowly to the mixture to terminate the reaction. GtO synthesis was completed within 1 h. The observed color of the mixture was dark brown. For purification, the resulting mixture was centrifuged at 3300 rpm for 15 min, where the oxidized graphite will sediment at the bottom of the centrifuging tube as pellets. After that, the graphite oxide pellets were rinsed with 5% HCl solution. Then, vacuum filtration was used to separate the graphite oxide from the supernatant by a membrane filter paper with a pore size of 11 μm.

2.4. Characterization. X-ray diffraction (XRD) patterns of oxidized graphite synthesis were determined by a D8 Advance ECO powder diffractometer (Bruker Corporation) using a high-brilliance 1 kW X-ray source. The Fourier transformed infrared (FTIR) spectrum was measured with a Bruker Vertex V80 V Vacuum FT-IR spectrometer coupled with an IR microscope and a mercury cadmium telluride (MCT) detector cooled with liquid nitrogen (Bruker Corporation) in the range of 400−4000 cm^{-1}. The microstructures of GtO sheets were investigated using inVia confocal Raman microscope (Renishaw) with a 488 nm laser beam. Optical microscope images were obtained using Axioskop 40 (ZEISS) and Hammamatsu ORCA CCD camera. Obtained images were processed using image processing and statistical tools in ImageJ. For sample characterization, the collected GtO product was vacuum-dried at low temperatures (45 °C) overnight. The dried products were subject to grinding before XRD, FTIR, and Raman analysis. The dried products were stored in a desiccator at vacuum conditions to avoid ambient moisture prior to characterization.

3. RESULTS AND DISCUSSION

In the TCR system, the hydrodynamic condition of the fluids is dependent on the Taylor number (Ta).[35] In this investigation, we carried out the oxidation of graphite in the TCR at five different hydrodynamic flow regimes:

(i) CF,
(ii) the onset of the primary instability (PI) between CF and TVF,
(iii) TVF,
(iv) the onset of the secondary instability (SI) between TVF and WVF,
(v) WVF.

TVF is a stable flow regime characterized by the presence of axisymmetric instabilities that leads into the formation of toroidal vortices, or Taylor rolls. As the rotation speed increases, the flow is transformed into WVF, which is an unstable flow regime characterized by the presence of nonaxisymmetric instabilities due to a traveling wave within the flow.[44] We note that at the onset of both primary and secondary instabilities, the flow condition transforms from one regime to another regime due to the increase in viscosity of the mixture. This causes the mixture to experience unstable and nonhomogeneous flow conditions in TCR. The hydrodynamic flow regimes investigated are shown in Figure 2. Table 2 shows the ratio between the Taylor number and the critical Taylor number for each flow regime at the inlet and the outlet. Given the gradual increase in viscosity, the critical point at which the flow starts transforming from TVF to CF (Figure 2b) is around 14 cm from the inlet. Similarly, the critical point at which the

Table 2. Ta/Ta_c Ratios for Flow Regimes in Taylor−Couette Reactor System

flow regime	CF	PI	TVF	SI	WVF
$Ta/Ta_{c,inlet}$	0.72	1.04	1.16	1.42	2.90
$Ta/Ta_{c,outlet}$	0.66	0.95	1.06	1.29	2.64
GtO	GtO-1	GtO-2	GtO-3	GtO-4	GtO-5

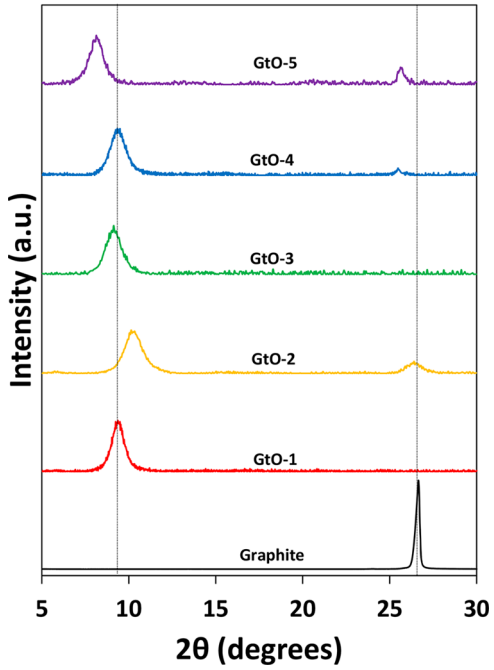

Figure 3. X-ray diffraction patterns of natural graphite and GtO samples synthesized in continuous Taylor−Couette reactor system with respect to flow regimes.

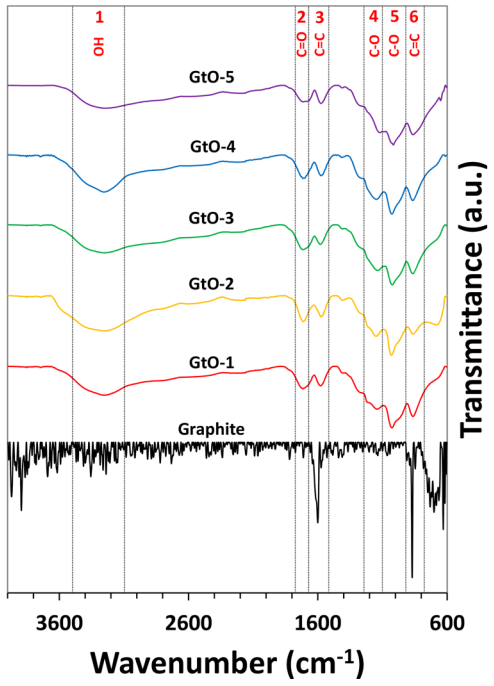

Figure 4. Fourier transform infrared spectra of natural graphite and GtO samples synthesized in continuous Taylor−Couette reactor system with respect to flow regime.

DOI: 10.1021/acs.iecr.8b04428
Ind. Eng. Chem. Res. 2019, 58, 1167−1176

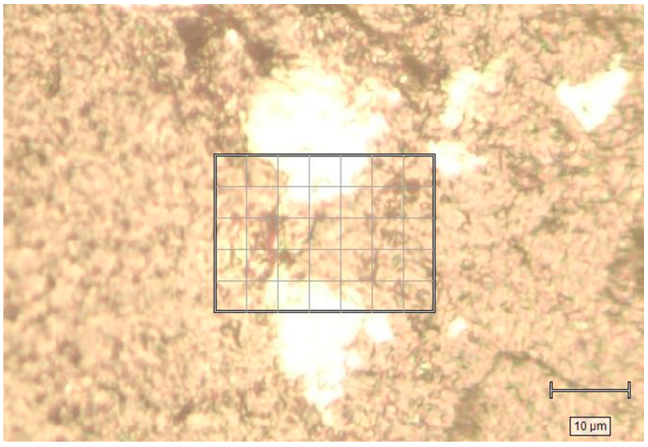

Figure 5. Optical microscope image of GtO sample in powder form on a glass substrate used in image acquisition mode for Raman spectroscopy.

flow starts transforming from WVF to TVF (Figure 2d) is around 12 cm from the inlet.

3.1. X-ray Diffraction (XRD) Analysis. XRD analysis was used to investigate structural crystallinity of the synthesized GtO samples. Figure 3 compares XRD patterns for the samples with respect to the flow regime. XRD patterns correspond to the interlayer spacing according to Bragg's law. Graphite has the main peak at 26.66° 2θ corresponding to the interlayer spacing of ~0.34 nm. After oxidation, the graphite structure is modified with the addition of oxygenated functional groups, which increases the interlayer spacing and moves the main XRD peaks toward the left. The new peak of 2θ at ~9.23° corresponds to an oxidized graphite structure with an interlayer spacing of ~0.95 nm. The new peak of 2θ may reflect the degree of oxidation in which the highest oxidation degree could correspond to the largest interlayer spacing. On the other hand, the interlayer spacing is variable in GtO sample reported in the literature depending on synthesis methods, air moisture content, drying methods, and other factors.[45] The variability in the interlayer spacing between GtO samples could be attributed to the perturbation of the oxygen functional groups bound to the graphitic basal plane and the presence of water molecules between the graphene sheets.[46] We note that in the presence of inhomogeneity in the flow structure in PI and SI and in the WVF regime, the characteristic graphite peak is still present, whereas the graphite peak completely disappears in CF (GtO-1) and TVF (GtO-3) cases. This indicates that the laminar CF and TVF regimes result in higher oxidation levels of graphite flakes. The peaks corresponding to graphite oxide (2θ ~9.23°) were much broader in comparison to the characteristic graphite peak (2θ ~ 26.66°). This indicates an exfoliation of the graphene sheets from the precursor structure caused by the formation of oxygenated functional groups and the wall shear exfoliation induced by the rotation of the inner cylinder. This corresponds to a significant decrease in the crystallite length along the *c*-axis in the graphite structure and a decrease in the number of layers.[47,48] The number of layers decreases from ~85 layers (natural graphite) to ~8 layers, as determined by the Scherrer formula.

3.2. Fourier Transform Infrared (FTIR) Spectroscopy. The produced GtO has oxygenated functional groups in its graphitic sheets: carboxyl (COOH), carbonyl (—C═O), epoxy (C—O—C), and hydroxyl (—OH) groups on the graphene sheet basal plane and edges.[49] Figure 4 shows the FTIR spectra of the samples to show the existence of the different oxygenated functional groups. There are six main peaks centered at 865, 1025, 1060, 1580, 1715, and 3240 cm^{-1}. The peaks at 865 and 1580 cm^{-1} denote the presence skeletal vibration from unoxidized graphitic domain (C═C). The peaks at 1025 and 1060 cm^{-1} correspond to epoxy (C—O—C) and carboxyl (COOH) groups. The peak at 1715 cm^{-1} arises from the vibrational mode of carbonyl (—C═O) groups. The broad peak at 3240 cm^{-1} indicates the presence of OH stretching in carboxyl (COOH) and hydroxyl (—OH) groups. Thus, the FTIR spectra verify the significant existence of various oxygenated functional groups in the produced graphite oxide samples. We note that the formation of the oxygenated functional groups is independent of the flow structure given that the same oxidizing agents are used in the synthesis.

3.3. Raman Spectroscopy. Raman spectroscopy can be used as a noninvasive method to characterize graphitic properties such as disorder, edge and grain boundaries, thickness, and exfoliation. Raman spectoscopy for all samples was carried out using a map image acquisition mode to test for structural properties and homogeneity in different graphite oxide samples. Image acquisition mode focused the laser to a spot and moves the sample under the laser using a motorized stage, which results in an array of sample points spanning the defined region of interest, as shown in Figure 5. Energy shift caused by laser excitation creates main peak positions: D band (1350 cm^{-1}), G band (1570 cm^{-1}), and 2D band (2700 cm^{-1}). Exposing graphite flakes to strong oxidizing agents and the formation of oxygenated functional groups result in structural changes in graphite lattice at the basal plane and at the edges. Oxidizing graphite contributes to the formation of defects and disorders that result in a higher intensity of the D band. The intensity of the D band increases with increasing oxidation. The G band position is due to first-order scattering of the E2g mode of vibration and shifts toward higher wavenumber with an increase in oxidation level. The G band position will reach 1600 cm^{-1} at highest level of oxidation due to the formation of new sp^3 carbon atoms in graphitic lattice. The full-width-at-half-maximum (fwhm) of the G band increases with increasing oxidation level due to the presence of sp^3 carbon atoms. The 2D band is used to evaluate the structural parameters of the *c*-axis orientation and exfoliation levels. The 2D band increases in intensity after oxidation due to the exfoliation of graphene sheets. The intensity of the 2D band increases with increasing exfoliation levels and broadens at higher oxidation levels. A new band at 2950 cm^{-1} called the D + G band starts appearing at increasing oxidation levels that illustrates disruption in graphitic stacking order. The $I_{(D)}/I_{(G)}$ ratio is used to determine oxidation levels. The $I_{(D)}/I_{(G)}$ ratio increases with increasing oxidation levels and becomes saturated at highest oxidation levels. The $I_{(2D)}/I_{(G)}$ ratio is used to illustrate the transition from crystalline to an amorphous phase upon oxidation of graphite flakes.[50] Figure 6 shows two representations of the Raman spectra (E_{Laser} = 488 nm) of natural graphite and the five GtO samples in powder form. It shows that the graphite precursor (Figure 6a) and GtO-3 (Figure 6d) have a high level of homogeneity in terms of stacking uniformity and disorder. It also confirms that TVF conditions used in synthesizing GtO-3 have preserved the stacking properties of natural graphite and resulted in a homogeneous graphite oxide sample in comparison to other flow conditions.

DOI: 10.1021/acs.iecr.8b04428
Ind. Eng. Chem. Res. 2019, 58, 1167−1176

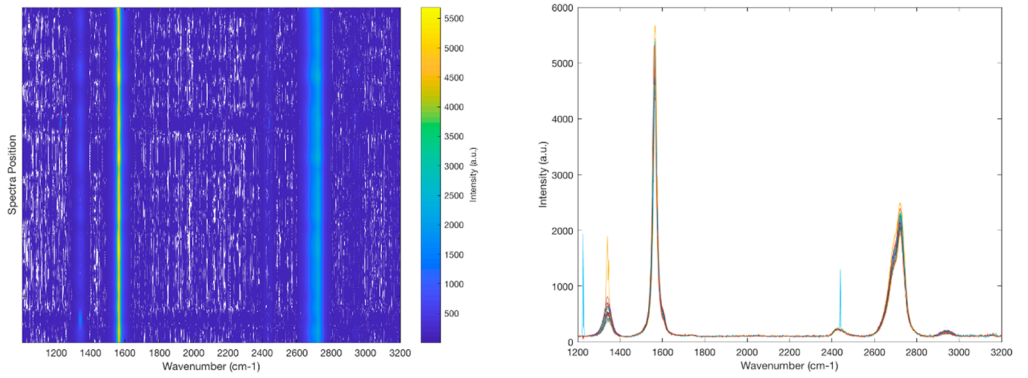

(a) Graphite

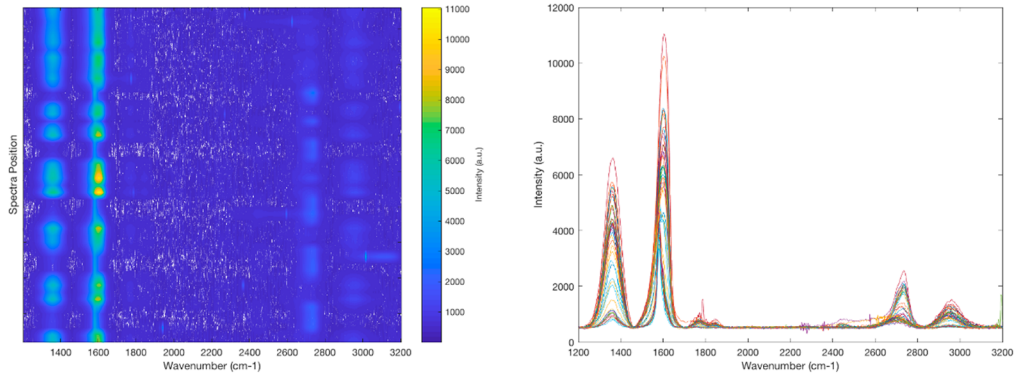

(b) GtO-1

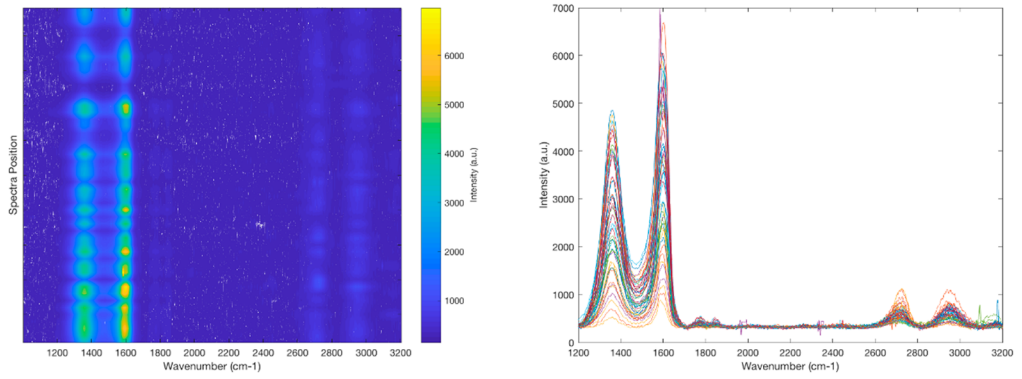

(c) GtO-2

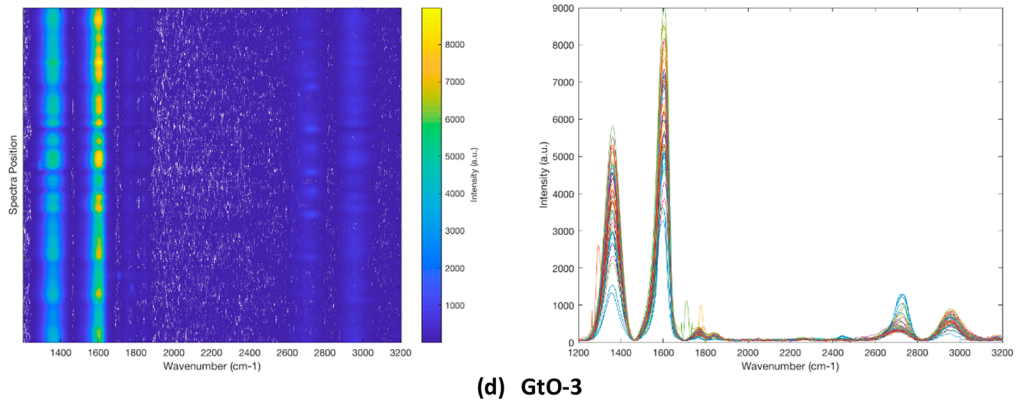

(d) GtO-3

Figure 6. continued

DOI: 10.1021/acs.iecr.8b04428
Ind. Eng. Chem. Res. 2019, 58, 1167−1176

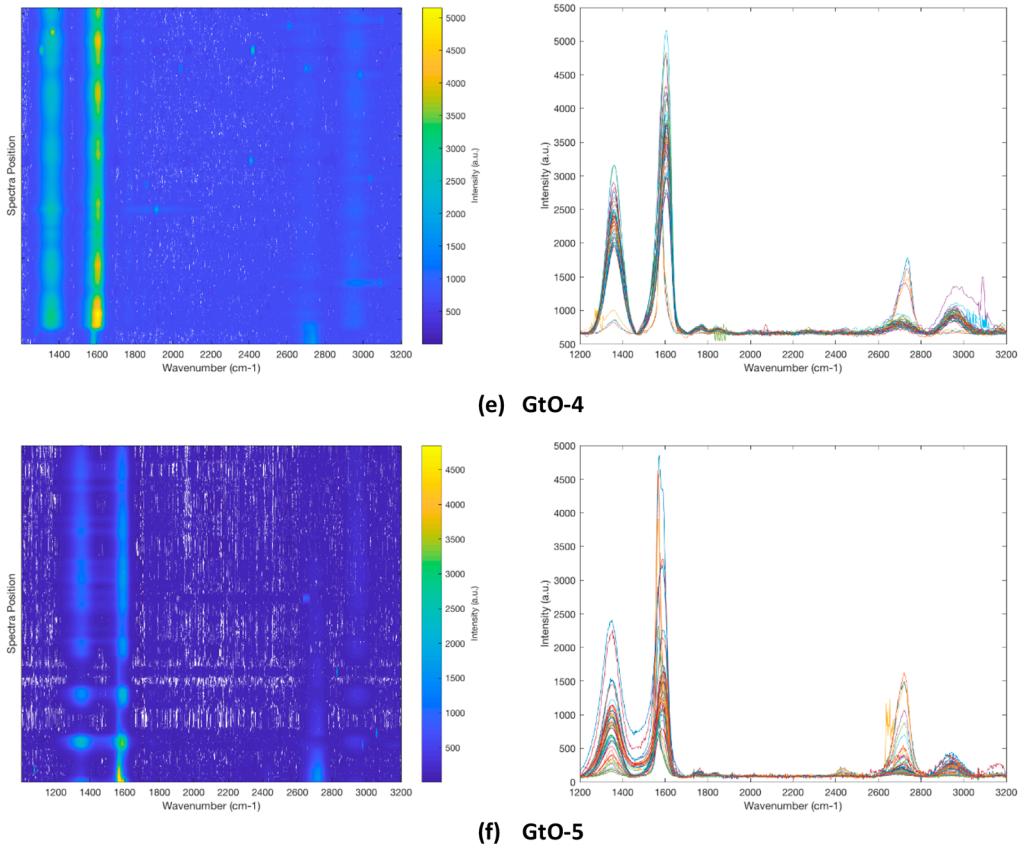

Figure 6. Raman spectroscopy of natural graphite and GtO samples synthesized in continuous Taylor−Couette reactor system with respect to flow regime.

Figure 7a shows the resultant changes in the G peak position and G peak fwhm with respect to flow regimes used for the synthesis. It elucidates that the G band is shifted toward a higher wavenumber and a considerable increase in fwhm with respect to oxidation level associated with the flow regime. It suggests that GtO-3 has the highest oxidation level at G peak position of ∼1600 cm^{-1} and high fwhm levels resulting from an increased formation of new sp^3 carbon atoms. Figure 7b represents the variation of $I_{(D)}/I_{(G)}$ ratio and $I_{(2D)}/I_{(G)}$ ratio with respect to flow regimes where both ratios increase at high oxidation levels. It indicates that GtO-3 has a high oxidation level at $I_{(D)}/I_{(G)}$ (∼0.79) and $I_{(2D)}/I_{(G)}$ (∼1.69) ratios. We note that the $I_{(2D)}/I_{(G)}$ ratios of the synthesized samples remain within 10% difference from the $I_{(2D)}/I_{(G)}$ ratio of the natural graphite precursor due to the preservation of the stacking properties of natural graphite. Significantly small error tolerance in GtO-3 suggests that TVF is an efficient flow regime that produces a homogeneous GtO product. It should be noted that despite almost 75% higher rotation speed than TVF, and thus increased energy consumption, GtO-5 from WVF exhibits much lower level of oxidation and much higher standard deviation, illustrating the importance of utilization of the appropriate flow structure in continuous TCR to maximize oxidization with homogeneity in the product.

3.4. Morphological Characterization. The synthesized GtO samples were diluted in deionized (DI) water, and the surface morphology of the samples was investigated using optical microscopy as shown in Figure 8. It was found that synthesized GtO sheets form random aggregations of crumbled thin sheets. GtO sheets possess different transparency levels due to the number of layers present in the stacked structure of GtO. The number of layers in GtO sheets can be easily detected by the difference in contrast between the sheets. Single- and few-layered graphene oxide sheets were observed to be more transparent than multilayered and underoxidized graphene sheets.[50] Table 3 shows the average size of graphite and GtO flakes in DI water. It was found that the continuous high shear applied in CF resulted in smaller GtO sheets. The applied shear and consistent Taylor vortex formation in TVF resulted in smaller GtO flakes in comparison to the graphite precursor. WVF produces aggregates of GtO flakes larger than the graphite precursor due to inconsistent turbulent vortex boundaries. We note that the presence turbulence in the operating flow condition results in the formation of aggregates of GtO flakes as can be seen in Table 3. This is due to the nature of turbulent mixing and nonaxisymmetric instabilities that results in the application of inconsistent shear gradient to GtO flakes.

4. CONCLUSION

The current study on continuously producing GtO, a precursor to GO, using a Taylor−Couette flow reactor system demonstrates the influence of flow regime and the presence of inhomogeneity within the flow structure on oxidation levels. In summary, the level of oxidation increased at the TVF flow regime and significantly decreased after the secondary instability at the WVF flow regime. The presence of an instability in PI and SI resulted in a nonhomogeneous flow condition that leads to lower oxidation levels. Moreover, the results obtained from WVF clearly show how nonhomoge-

DOI: 10.1021/acs.iecr.8b04428
Ind. Eng. Chem. Res. 2019, 58, 1167−1176

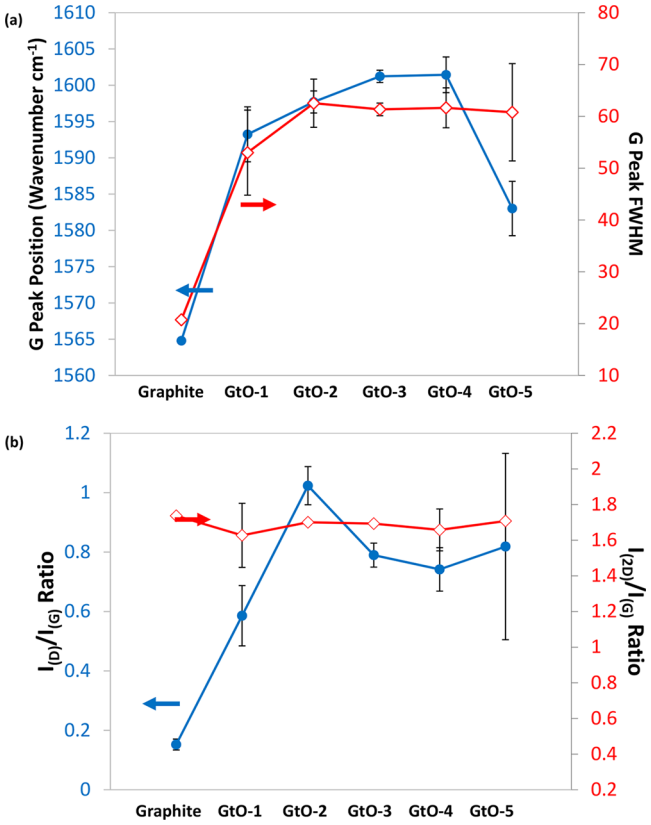

Figure 7. (a) G band position and fwhm of GtO samples of varying flow conditions. (b) $I_{(D)}/I_{(G)}$ ratio and $I_{(2D)}/I_{(G)}$ ratio of GtO samples of varying flow conditions.

neous, turbulent mixing and the presence of nonaxisymmetric instabilities in a continuous TCR resulted in lower oxidation levels. More importantly, continuous TVF flow regime resulted in a structurally uniform graphite oxide product that can be used in a variety of applications, including energy storage and catalysis. The reported method serves as an advantageous step into large-scale production of GO for potential use in various downstream processes.

AUTHOR INFORMATION

Corresponding Author

*Address: 113 Ho Plaza, 340 Olin Hall, Cornell University, Ithaca, NY 14853. Tel.: +1 607 255 8591. E-mail: ylj2@cornell.edu.

ORCID

Yong Lak Joo: 0000-0002-4646-1625

Notes

The authors declare no competing financial interest.

ACKNOWLEDGMENTS

The authors acknowledge Axium Nano, LLC for the partial support of this work (Cornell OSP No. 89675). This work made use of the Cornell Center for Materials Research Shared Facilities, which are supported through the NSF MRSEC program (DMR-1719875). The authors also acknowledge the Cornell Laboratory of Atomic and Solid-State Physics Machine Shop for manufacturing the TCR setup and Asbury Carbons for providing graphite samples. M.A. acknowledges Saudi Aramco's Advanced Degree Program. This research was partly supported by the Basic Science Research program of the National Research Foundation of Korea (NRF), funded by the Ministry of Education, Science, and Technology (2016R1A6A1A03012069).

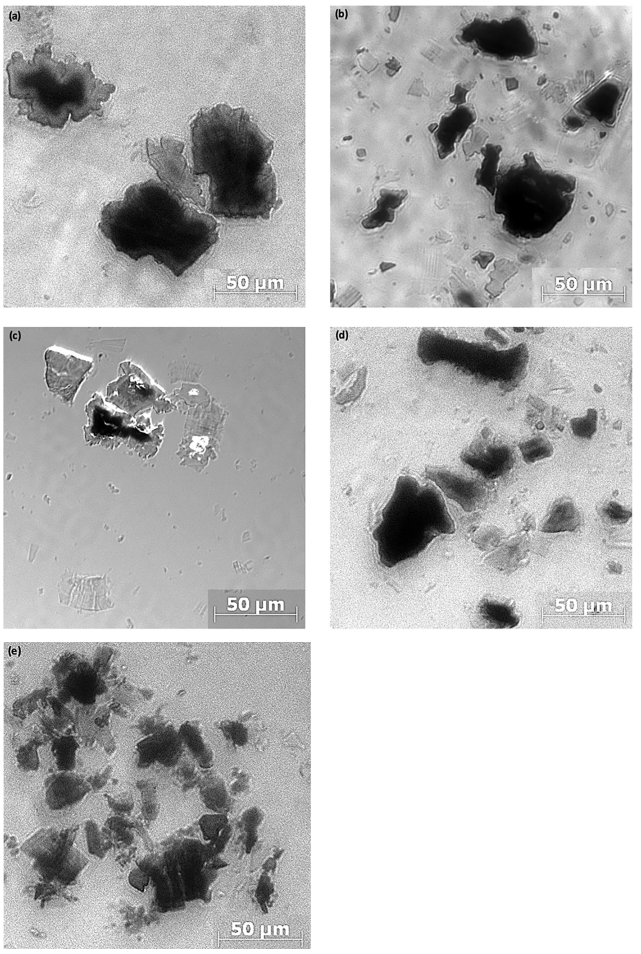

Figure 8. Optical microscope images of (a) GtO-1, (b) GtO-2, (c) GtO-3, (d) GtO-4, and (e) GtO-5.

Table 3. Average Size of Graphite and GtO Flakes

sample	graphite precursor	GtO-1	GtO-2	GtO-3	GtO-4	GtO-5
average area (μm^2)	117.9	79.4	68.7	88.0	120.6	179.7

REFERENCES

(1) Liu, C.; Li, F.; Ma, L. P.; Cheng, H. M. Advanced Materials for Energy Storage. *Adv. Mater.* **2010**, *22* (8), E28−E62.

(2) Jing, S.; Jiang, H.; Hu, Y.; Li, C. Graphene supported mesoporous single crystal silicon on Cu foam as a stable lithium-ion battery anode. *J. Mater. Chem. A* **2014**, *2* (39), 16360−16364.

(3) van Schalkwijk, W. A.; Scrosati, B. *Advances in Lithium-Ion Batteries*; Springer: Boston, MA, 2004.

(4) Beaulieu, L. Y.; Hatchard, T. D.; Bonakdarpour, A.; Fleischauer, M. D.; Dahn, J. R. Reaction of Li with alloy thin films studied by in situ AFM. *J. Electrochem. Soc.* **2003**, *150* (11), A1457−A1464.

(5) Kasavajjula, U.; Wang, C.; Appleby, A. Nano- and bulk-silicon-based insertion anodes for lithium-ion secondary cells. *J. Power Sources* **2007**, *163*, 1003.

(6) Huggins, R. A.; Nix, W. D. Decrepitation model for capacity loss during cycling of alloys in rechargeable electrochemical systems. *Ionics* **2000**, *6*, 57.

DOI: 10.1021/acs.iecr.8b04428
Ind. Eng. Chem. Res. 2019, 58, 1167−1176

(7) Yu, Y.; Gu, L.; Zhu, C.; Tsukimoto, S.; van Aken, P. A.; Maier, J. Reversible Storage of Lithium in Silver-Coated Three-Dimensional Macroporous Silicon. *Adv. Mater.* **2010**, *22* (20), 2247.
(8) Chou, S.-L.; Wang, J.-Z.; Choucair, M.; Liu, H.-K.; Stride, J. A.; Dou, S.-X. Enhanced reversible lithium storage in a nanosize silicon/graphene composite. *Electrochem. Commun.* **2010**, *12* (2), 303−306.
(9) Boukamp, B. A.; Lesh, G. C.; Huggins, R. A. All-solid lithium electrodes with mixed-conductor matrix. *J. Electrochem. Soc.* **1981**, *128* (4), 725−729.
(10) Liu, N.; Lu, Z. D.; Zhao, J.; McDowell, M. T.; Lee, H. W.; Zhao, W. T.; Cui, Y. A pomegranate-inspired nanoscale design for large-volume-change lithium battery anodes. *Nat. Nanotechnol.* **2014**, *9* (3), 187−192.
(11) Xiang, H. F.; Zhang, K.; Ji, G.; Lee, J. Y.; Zou, C. J.; Chen, X. D.; Wu, J. S. Graphene/nanosized silicon composites for lithium battery anodes with improved cycling stability. *Carbon* **2011**, *49* (5), 1787−1796.
(12) Fei, L.; Yoo, S. H.; Villamayor, R. A.; Williams, B. P.; Gong, S.; Park, S.; Shin, K.; Joo, Y. L. Graphene Oxide Involved Air-controlled Electrospray for Uniform, Ultrafast, Instantly-Dry, and Binder-Free Electrode Fabrication. *ACS Appl. Mater. Interfaces* **2017**, *9* (11), 9738−9746.
(13) Novoselov, K. S.; Jiang, D.; Schedin, F.; Booth, T. J.; Khotkevich, V. V.; Morozov, S. V.; Geim, A. K. Two-dimensional atomic crystals. *Proc. Natl. Acad. Sci. U. S. A.* **2005**, *102* (30), 10451−10453.
(14) Stankovich, S.; Dikin, D. A.; Dommett, G. H. B.; Kohlhaas, K. M.; Zimney, E. J.; Stach, E. A.; Piner, R. D.; Nguyen, S. T.; Ruoff, R. S. Graphene-based composite materials. *Nature* **2006**, *442* (7100), 282−286.
(15) Geim, A. K.; Novoselov, K. S. The rise of graphene. *Nat. Mater.* **2007**, *6* (3), 183−191.
(16) Si, Y. C.; Samulski, E. T. Exfoliated Graphene Separated by Platinum Nanoparticles. *Chem. Mater.* **2008**, *20* (21), 6792−6797.
(17) Zhu, Y.; Murali, S.; Cai, W.; Li, X.; Suk, J. W.; Potts, J. R.; Ruoff, R. S. Graphene and Graphene Oxide: Synthesis, Properties, and Applications. *Adv. Mater.* **2010**, *22* (35), 3906−3924.
(18) Machado, B. F.; Serp, P. Graphene-based materials for catalysis. *Catal. Sci. Technol.* **2012**, *2* (1), 54−75.
(19) Wang, Z. Y.; Li, F.; Ergang, N. S.; Stein, A. Effects of hierarchical architecture on electronic and mechanical properties of nanocast monolithic porous carbons and carbon-carbon nanocomposites. *Chem. Mater.* **2006**, *18* (23), 5543−5553.
(20) Hassan, F. M.; Elsayed, A. R.; Chabot, V.; Batmaz, R.; Xiao, X. C.; Chen, Z. W. Subeutectic Growth of Single-Crystal Silicon Nanowires Grown on and Wrapped with Graphene Nanosheets: High-Performance Anode Material for Lithium-Ion Battery. *ACS Appl. Mater. Interfaces* **2014**, *6* (16), 13757−13764.
(21) Novoselov, K. S.; Geim, A. K.; Morozov, S. V.; Jiang, D.; Zhang, Y.; Dubonos, S. V.; Grigorieva, I. V.; Firsov, A. A. Electric field effect in atomically thin carbon films. *Science* **2004**, *306* (5696), 666−669.
(22) Reina, A.; Jia, X.; Ho, J.; Nezich, D.; Son, H.; Bulovic, V.; Dresselhaus, M. S.; Kong, J. Large Area, Few-Layer Graphene Films on Arbitrary Substrates by Chemical Vapor Deposition. *Nano Lett.* **2009**, *9* (1), 30−35.
(23) Li, X.; Cai, W.; An, J.; Kim, S.; Nah, J.; Yang, D.; Piner, R.; Velamakanni, A.; Jung, I.; Tutuc, E.; Banerjee, S. K.; Colombo, L.; Ruoff, R. S. Large-Area Synthesis of High-Quality and Uniform Graphene Films on Copper Foils. *Science* **2009**, *324* (5932), 1312−1314.
(24) Berger, C.; Song, Z. M.; Li, T. B.; Li, X. B.; Ogbazghi, A. Y.; Feng, R.; Dai, Z. T.; Marchenkov, A. N.; Conrad, E. H.; First, P. N.; de Heer, W. A. Ultrathin epitaxial graphite: 2D electron gas properties and a route toward graphene-based nanoelectronics. *J. Phys. Chem. B* **2004**, *108* (52), 19912−19916.
(25) Kim, K. S.; Zhao, Y.; Jang, H.; Lee, S. Y.; Kim, J. M.; Ahn, J. H.; Kim, P.; Choi, J. Y.; Hong, B. H.; Kim, K.S. Large-scale pattern growth of graphene films for stretchable transparent electrodes. *Nature* **2009**, *457* (7230), 706−710.
(26) Brodie, B. C. *Ann. Chim. Phys.* **1860**, *56*, 466−472.
(27) Staudenmaier, L. *Ber. Dtsch. Chem. Ges.* **1898**, *31* (1481), 1481.
(28) Hummers, W. S.; Offeman, R. E. Preparation of graphitic oxide. *J. Am. Chem. Soc.* **1958**, *80* (6), 1339−1339.
(29) Marcano, D. C.; Kosynkin, D. V.; Berlin, J. M.; Sinitskii, A.; Sun, Z.; Slesarev, A.; Alemany, L. B.; Lu, W.; Tour, J. M. Improved Synthesis of Graphene Oxide. *ACS Nano* **2010**, *4* (8), 4806−4814.
(30) Chen, J.; Yao, B. W.; Li, C.; Shi, G. Q. An improved Hummers method for eco-friendly synthesis of graphene oxide. *Carbon* **2013**, *64*, 225−229.
(31) Shahriary, L.; Athawale, A. A. Graphene Oxide Synthesized by Using Modified Hummers Approach. *Int. J. Renew. Energy Environ. Eng.* **2014**, *02* (01), 58−63.
(32) Park, W. K.; Kim, H.; Kim, T.; Kim, Y.; Yoo, S.; Kim, S.; Yoon, D. H.; Yang, W. S. Facile synthesis of graphene oxide in a Couette-Taylor flow reactor. *Carbon* **2015**, *83*, 217−223.
(33) Taylor, G. I. Stability of a viscous liquid contained between two rotating cylinders. *Proc. R. Soc. London, Ser. A* **1923**, *102* (718), 541−542.
(34) Couette, M. Distinction de deux régimes dans le mouvement des fluids. *J. Phys. Theor. Appl.* **1890**, *9* (1), 414−424.
(35) Grossmann, S.; Lohse, D.; Sun, C. High-Reynolds Number Taylor-Couette Turbulence. *Annu. Rev. Fluid Mech.* **2016**, *48*, 53−80.
(36) Aljishi, M. F.; Ruo, A. C.; Park, J. H.; Nasser, B.; Kim, W. S.; Joo, Y. L. Effect of flow structure at the onset of instability on barium sulfate precipitation in Taylor-Couette crystallizers. *J. Cryst. Growth* **2013**, *373*, 20−31.
(37) Liu, C. I.; Lee, D. J. Micromixing effects in a couette flow reactor. *Chem. Eng. Sci.* **1999**, *54* (13−14), 2883−2888.
(38) Nemri, M.; Charton, S.; Climent, E. Mixing and axial dispersion in Taylor-Couette flows: The effect of the flow regime. *Chem. Eng. Sci.* **2016**, *139*, 109−124.
(39) Snyder, H. A. Experiments on the stability of spiral flow at low axial Reynolds numbers. *Proc. R. Soc. London, Ser. A* **1962**, *265* (1321), 198−214.
(40) Kim, W. S. Application of Taylor Vortex to Crystallization. *J. Chem. Eng. Jpn.* **2014**, *47* (2), 115−123.
(41) Nguyen, A. T.; Kim, J. M.; Chang, S. M.; Kim, W. S. Taylor Vortex Effect on Phase Transformation of Guanosine 5-Monophosphate in Drowning-Out Crystallization. *Ind. Eng. Chem. Res.* **2010**, *49* (10), 4865−4872.
(42) Einstein, A. A new determination of molecular dimensions. *Ann. Phys.* **1906**, *19*, 289−306.
(43) Park, W. K.; Yoon, Y.; Kim, S.; Choi, S. Y.; Yoo, S.; Do, Y.; Jung, S.; Yoon, D. H.; Park, H.; Yang, W. S. Toward Green Synthesis of Graphene Oxide Using Recycled Sulfuric Acid via Couette-Taylor Flow. *ACS Omega* **2017**, *2* (1), 186−192.
(44) Marcus, P. S. Simulation of Taylor-Couette flow. 2. Numerical results for wavy-vortex flow with one traveling wave. *J. Fluid Mech.* **1984**, *146* (SEP), 65−113.
(45) Hontorialucas, C.; Lopezpeinado, A. J.; Lopezgonzalez, J. D. D.; Rojascervantes, M. L.; Martinaranda, R. M. Study of oxygen-containing groups in a series of graphite oxides - physical and chemical characterization. *Carbon* **1995**, *33* (11), 1585−1592.
(46) Peng, S. G.; Fan, X. J.; Li, S.; Zhang, J. Green synthesis and characterization of graphite oxide by orthogonal experiment. *J. Chilean Chem. Soc.* **2013**, *58* (4), 2213−2217.
(47) Chowdhury, D. R.; Singh, C.; Paul, A. Role of graphite precursor and sodium nitrate in graphite oxide synthesis. *RSC Adv.* **2014**, *4* (29), 15138−15145.
(48) Lee, D. W.; De Los Santos, V. L.; Seo, J. W.; Felix, L. L.; Bustamante, D. A.; Cole, J. M.; Barnes, C. H. W. The Structure of Graphite Oxide: Investigation of Its Surface Chemical Groups. *J. Phys. Chem. B* **2010**, *114* (17), 5723−5728.
(49) Chowdhury, S.; Balasubramanian, R. Recent advances in the use of graphene-family nanoadsorbents for removal of toxic pollutants from wastewater. *Adv. Colloid Interface Sci.* **2014**, *204*, 35−56.

DOI: 10.1021/acs.iecr.8b04428
Ind. Eng. Chem. Res. 2019, 58, 1167−1176

(50) Krishnamoorthy, K.; Veerapandian, M.; Yun, K.; Kim, S. J. The Chemical and structural analysis of graphene oxide with different degrees of oxidation. *Carbon* **2013**, *53*, 38−49.

DOI: 10.1021/acs.iecr.8b04428
Ind. Eng. Chem. Res. 2019, 58, 1167−1176